Foreword by Chih-Ming Ho

Fluid flow through small channels has become a popular research topic due to the emergence of biochemical lab-on-the-chip systems and micro electromechanical system fabrication technologies, which began in the late 1980s. This book provides a comprehensive summary of using computational tools (Chapters 14–18) to describe fluid flow in micro and nano configurations. Although many fundamental issues that are not observed in macro flows are prominent in microscale fluid dynamics, the flow length scale is still much larger than the molecular length scale, allowing for the continuum hypothesis to still hold in most cases (Chapter 1). However, the typical Reynolds number is much less than unity, due to the small transverse length scale, which results in a high-velocity gradient. For example, a $10^5\,\mathrm{sec}^{-1}$ shear rate is not an uncommon operating condition, and thus high viscous forces are prevalent, resulting in hundreds or thousands of ψ hydrodynamic pressure drops across a single fluidic network. Consequently, it is not a trivial task to design micropumps that are able to deliver the required pressure head without suffering debilitating leakage. Electrokinetic and surface tension forces (Chapters 7 and 8) are used as alternatives to move the embedded particles and/or bulk fluid. The high viscous damping also removes any chance for hydrodynamic instabilities, which are essential for effective mixing. Mixing in micro devices is often critical to the overall system's viability (Chapter 9). Using electrokinetic force to reach chaotic mixing is an interesting research topic. In these cases, the electrical properties, e.g., dielectric constants, rather than the viscosity determine the efficiency of transport.

The National Nano Initiative, established first in the USA (www.nano.gov)

and subsequently in many other countries, has pushed the length scale range of interest from microns down to nanometers. Flows in these regimes start to challenge the fundamental assumptions of continuum mechanics (Chapter 1). The effects of the molecules in the bulk of the fluid versus those molecules in proximity to a solid boundary become differentiated (Chapter 10). These are extremely intriguing aspects to be investigated for flows in small configurations. The demarcation between the continuum and the noncontinuum boundary has yet to be determined and inevitably will have a tremendous influence on the understanding of small-scale fluid behavior as well as system design.

The ratio between the size of the channel and that of the molecule is not the only parameter that validates the continuum assumption. In biological applications, for example, molecules with large conformation changes, electrical charges, and polar structures are frequently encountered. These variables make it impossible to determine whether a flow can be considered a continuum based only on a ratio of sizes (Chapter 11). When a continuum flow of a Newtonian fluid is assumed, molecular effects are defined by the governing equations of traditional fluid mechanics. Interactions among fluid molecules are expressed by a physical constant, which is viscosity. The no-slip condition represents the interactions between the fluid and the solid surface molecules. Both viscosity and the no-slip condition are concepts developed under the framework of continuum. Deviations from the bulk viscosity and the no-slip condition can lead to other results due to the breakdown of the continuum assumption (Chapters 2 and 10).

In the nanoflow regime, not many molecules are situated far away from the channel wall. Therefore, the motion of the bulk fluid is significantly affected by the potential fields generated by the molecules near the solid wall. Near the surface, the fluid molecules do not flow freely. At a distance of a few fluid molecule layers above the surface, the flow has very different physical constants from the bulk flow. The surface effects are strong not only in nano configurations (Chapter 10); even in microfluidic devices, the performance, e.g., surface fouling, is dependent on the surface property. We frequently spend more time on modifying the surface properties than on designing and fabricating devices. As a result of our limited understanding of fluidic behavior within nanoscale channels (Chapters 10 through 13), many vital systematic processes of today's technology are arduously, yet imperfectly, designed. Delivering and stopping a picoliter volume of fluid to a precise location with high accuracy as well as the separation and mixing of nano/micro particles in a fluid medium of high ionic concentration remains a challenging task. By furthering the understanding of fluid interactions in the nano world, many of the interesting mysteries and challenges that have puzzled scientists will be revealed.

June 2004, Los Angeles, California, USA Chih-Ming Ho

Preface

In the early 1990s, microchannel flow experiments at the University of Pennsylvania by the groups of H. Bau and J. Zemel revealed intriguing results for both liquids and gases that sparked excitement and new interest in the study of low Reynolds number flows in microscales. Another influential development at about the same time was the fabrication of the first microchannel with integrated pressure sensors by the groups of C.M. Ho (UCLA) and Y.C. Tai (Caltech). While the experimental results obtained at the University of Pennsylvania indicated global deviations of microflows from canonical flows, pointwise measurements for gas flows with pressure sensors, and later with temperature sensors, revealed a new flow behavior at microscales not captured by the familiar continuum theory. In microgeometries the flow is *granular* for liquids and *rarefied* for gases, and the walls "move." In addition, other phenomena such as thermal creep, electrokinetics, viscous heating, anomalous diffusion, and even quantum and chemical effects may become important. Most important, the material of the wall and the quality of its surface play a very important role in the momentum and energy exchange. One could argue that at least for gases the situation is similar to low-pressure high-altitude aeronautical flows, which were studied extensively more than 40 years ago. Indeed, there is a similarity in a certain regime of the Knudsen number. However, most gas microflows correspond to a low Reynolds number and low Mach number, in contrast to their aeronautical counterparts. Moreover, the typical microgeometries are of very large aspect ratio, and this poses more challenges for numerical modeling, but also creates opportunities for obtaining semianalytical results. For liquids no such analogy exists and their dynamics in confined

microgeometries, especially at the submicron range, is much more complex.

The main differences between fluid mechanics at microscales and in the macrodomain can be broadly classified into four areas:

- Noncontinuum effects,
- surface-dominated effects,
- low Reynolds number effects, and
- multiscale and multiphysics effects.

Some of these effects can be simulated with relatively simple modifications of the standard numerical procedures of computational fluid dynamics. However, others require new simulation approaches not used typically in the macrodomain, based on multiscale algorithms. For gas microflows, compressibility effects are very important because of relatively large density gradients, although the Mach number is typically low. Depending on the degree of rarefaction, corrections at the boundary or everywhere in the domain need to be incorporated. Increased rarefaction effects may make the constitutive models for the stress tensor and the heat flux vector in the Navier–Stokes equations invalid. On the other hand, working with the Boltzmann equation or with molecular dynamics implementation of Newton's law directly is computationally prohibitive for complex microgeometries. The same is true for liquids, since atomistic simulation based on Newton's law for individual atoms is restricted to extremely small volumes. Therefore, mesoscopic and hybrid atomistic–continuum methods need to be employed for both gas and liquid microflows to deal effectively with deviations from the continuum and to provide a link with the large domain sizes. Most important, microflows occur in devices that involve simultaneous action in the flow, electrical, mechanical, thermal, and other domains. This, in turn, implies that fast and flexible algorithms and low-dimensional modeling are required to make full-system simulation feasible, similar to the achievements of the 1980s in VLSI simulation.

There has been significant progress in the development of microfluidics and nanofluidics at the application as well as at the fundamental and simulation levels since the publication of an earlier volume of this book (2001). We have, therefore, undertaken the "nontrivial" task of updating the book in order to include these new developments. The current book covers length scales from angstroms to microns (and beyond), while the first volume covered scales from one hundred nanometers to microns (and beyond). We have maintained the emphasis on fundamental concepts with a mix of semi-analytical, experimental, and numerical results, and have outlined their relevance to modeling and analyzing functional devices. The first two co-authors (GK and AB) are very pleased to have a new co-author, Prof. N.R. Aluru, whose unique contributions have made this new volume pos-

sible. We are also grateful to Springer, and in particular to Senior Editor in Mathematics Dr. Achi Dosanjh, who gave us this opportunity.

The majority of the new developments are in Chapters 7 through 18, most of which contain totally new material. In addition, all other Chapters (1 through 6) have been modified, and in some cases new material has also been added. We have divided the material into three main categories by subject:

1. Gas Flows (Chapters 2–6).
2. Liquid Flows (Chapters 7–13)
3. Simulation Techniques (Chapters 14–18)

The last category also contains two Chapters (17 and 18) on low-dimensional modeling and simulation, in addition to chapters on multiscale modeling of gas and liquid flows. The entire material can be used in a two-semester first- or second-year graduate course. Also, selected chapters can be used for a short course or an undergraduate-level course.

In the following we present a brief overview of the material covered in each chapter.

In Chapter 1 we provide highlights of the many concepts and devices that we will discuss in detail in the subsequent chapters. For historic reasons, we start with some prototype Micro-Electro-Mechanical-Systems (MEMS) devices and discuss such fundamental concepts as breakdown of constitutive laws, new flow regimes, and modeling issues encountered in microfluidic and nanofluidic systems. We also address the question of full-system simulation of microsystems and introduce the concept of macromodeling.

In Chapter 2 we first present the basic equations of fluid dynamics for both incompressible and compressible flows, and discuss appropriate nondimensionalizations. Subsequently, we consider the compressible Navier–Stokes equations and develop a general boundary condition for velocity slip. The validity of this model is assessed in subsequent chapters.

In Chapter 3 we consider shear-driven gas flows with the objective of modeling several microsystem components. In order to circumvent the difficulty of understanding the flow physics for complex engineering geometries, we concentrate on prototype flows such as the linear and oscillatory Couette flows in the slip, transition, and free-molecular flow regimes, and flow in shear-driven microcavities and microgrooves.

In Chapter 4 we present pressure-driven gas flows in the slip, transition and free molecular flow regimes. In the slip flow regime, we first validate simulation results based on compressible Navier–Stokes solutions employing various slip models introduced in Chapter 2. In addition, we examine the accuracy of the one-dimensional Fanno theory for microchannel flows, and we study inlet flows and effects of roughness. In the transition and free-molecular regime we develop a unified model for predicting the velocity

profile and mass flowrate for pipe and duct flows.

In Chapter 5 we consider heat transfer in gas microflows. In the first section we concentrate on the thermal creep (transpiration) effects that may be important in channels with tangential temperature gradients on their surfaces. We also study other temperature-induced flows and investigate the validity of the heat conduction equation in the limit of zero Knudsen number. In the second and third sections we investigate the combined effects of thermal creep, heat conduction, and convection in pressure-, force-, and shear-driven channel flows.

In Chapter 6 we consider rarefied gas flows encountered in applications other than simple microchannels. In the first section, we present the lubrication theory and its application to the slider bearing and squeezed film problems. In the second and third sections, we consider separated flows in internal and external geometries in the *slip flow* regime in order to investigate the validity of continuum-based slip models under flow separation. In the fourth section, we present theoretical and numerical results for Stokes flow past a sphere including rarefaction effects. In the fifth section we summarize important results on gas flows through microfilters used for capturing and detecting airborne biological and chemical particles. In the last section, we consider high-speed rarefied flows in micronozzles, which are used for controlling the motion of microsatellites.

In Chapter 7 we present basic concepts and a mathematical formulation of microflow control and pumping using electrokinetic effects, which do not require any moving components. We cover electroosmotic and electrophoretic transport in detail both for steady and time-periodic flows, and we discuss simple models for the near-wall flow. We also present dielectrophoresis, which enables separation and detection of similar size particles based on their polarizability.

In Chapter 8 we consider surface tension-driven flows and capillary phenomena involving wetting and spreading of liquid thin films and droplets. For microfluidic delivery on open surfaces, electrowetting and thermocapillary along with dielectrophoresis have been employed to move continuous and discrete streams of fluid. A new method of actuation exploits optical beams and photoconductor materials in conjunction with electrowetting. Such electrically or chemically defined paths can be reconfigured dynamically using electronically addressable arrays that respond to electric potential, temperature, or laser beams and control the direction, timing, and speed of fluid droplets. In addition to the above themes, we also study bubble transport in capillaries including both classical theoretical results and more recent theoretical and experimental results for electrokinetic flows.

In Chapter 9 we consider micromixers and chaotic advection. In microchannels the flow is laminar and steady, so diffusion is controlled solely by the diffusivity coefficient of the medium, thus requiring excessive amounts of time for complete mixing. To this end, chaotic advection has been exploited in applications to accelerate mixing at very low speeds. Here, we

present the basic ideas behind chaotic advection, and discuss examples of passive and active mixers that have been used in microfluidic applications. We also provide effective quantitative measures of characterizing mixing.

In Chapter 10 we consider simple liquids in nanochannels described by standard Lennard–Jones potentials. A key difference between the simulation of the fluidic transport in confined nanochannels and at macroscopic scales is that the well-established continuum theories based on Navier–Stokes equations may not be valid in confined nanochannels. Therefore, atomistic scale simulations are required to shed fundamental insight on fluid transport. Here we discuss density distribution, diffusion transport, and validity of the Navier–Stokes equations. In the last section we discuss in detail the slip condition at solid–liquid interfaces, and present experimental and computational results as well as conceptual models of slip. We also revisit the lubrication problem and present the Reynolds–Vinogradova theory for hydrophobic surfaces.

In Chapter 11 we focus on water and its properties in various forms; this is one of the most actively investigated areas because of its importance in nature. The anomalies that exist in the bulk properties of water make it very interesting and challenging for research, and a vast deal of literature is already available. Even though water has been studied for more than 100 years now, its properties are far from understood. With the advances in fabrication of nanochannels that are only a few molecular diameters in critical dimension, the properties of water in confined nanochannels have recently received a great deal of attention. In this chapter, after introducing some definitions and atomistic models for water, we present the static and dynamic behavior of water in confined nanochannels.

In Chapter 12 we discuss the fundamentals and simulation of electroosmotic flow in nanochannels. The basic theory was covered in Chapter 7, so here the limitations of the continuum theory for electroosmotic flow in nanochannels are identified by presenting a detailed comparison between continuum and MD simulations. Specifically, the significance of the finite size of the ions and the discrete nature of the solvent molecules are highlighted. A slip boundary condition that can be used in the hydrodynamic theory for nanochannel electroosmotic flows is presented. Finally, the physical mechanisms that lead to the charge inversion and flow reversal phenomena in nanochannel electroosmotic flows are discussed.

In Chapter 13 we focus on functional fluids and on functionalized devices, specifically nanotubes. The possibility to target and precisely control the electrooptical as well as the mechanical properties of microstructures in a dynamic way using external fields has opened new horizons in microfluidics research including new concepts and protocols for micro- and nanofabrication. On the more fundamental level, systematic studies of paramagnetic particles or charged particles and their dynamics offer insight into the role of Brownian noise in microsystems as well as conceptual differences between deterministic and stochastic modeling. This is studied in the first

part of this chapter. In the second part of the chapter we study carbon nanotubes and their properties. Carbon nanotubes with diameters as small as 5–10 Å are comparable to the diameters encountered in biological ion channels. By *functionalizing* carbon nanotubes, it is possible to tune the surface properties of carbon nanotubes to investigate the function of a variety of ion channels. To enable such advances, it is important to understand how water, ions, and various electrolytes interact with carbon nanotubes and functionalized nanotubes.

In Chapter 14 we discuss representative numerical methods for continuum-based simulations. The significant geometric complexity of flows in microsystems suggests that finite elements are more suitable than finite differences, while high-order accuracy is required for efficient discretization. To this end, we focus on spectral element and meshless methods in stationary and moving domains. We also discuss methods for modeling particulate microflows and focus on the force coupling method, a particularly fast approach suitable for three-dimensional simulations. These methods represent three different classes of discretization philosophies and have been used with success in diverse applications of microsystems.

In Chapter 15 we discuss theory and numerical methodologies for simulating gas flows at the mesoscopic and atomistic levels. Such a description is necessary for gases in the transition and free-molecular regimes. First, we present the Direct Simulation Monte Carlo (DSMC) method, a stochastic approach suitable for gases. We discuss limitations and errors in the steady version of DSMC and subsequently present a similar analysis for the unsteady DSMC. In order to bridge scales between the continuum and atomistic scales we present the Schwarz iterative coupling algorithm and apply it to modeling microfilters. We then give an overview of the Boltzmann equation, describing in some detail gas–surface interactions, and include benchmark solutions for validation of numerical codes and of macromodels. A main result relevant to accurately bridging microdynamics and macrodynamics is the Boltzmann inequality, which we also discuss in the last section on lattice Boltzmann methods (LBM). These methods represent a "minimal" discrete form of the Boltzmann equation, and they are applicable to both compressible and incompressible flows; in fact, the majority of LBM applications focuses on incompressible flows.

In Chapter 16 we discuss theory and numerical methodologies for simulating liquid flows at the atomistic and mesoscopic levels. The atomistic description is necessary for liquids contained in domains with dimension of fewer than ten molecules. First, we present the Molecular Dynamics (MD) method, a deterministic approach suitable for liquids. We explain details of the algorithm and focus on the various potentials and thermostats that can be used. This selection is crucial for reliable simulations of liquids at the nanoscale. In the next section we consider various approaches in coupling atomistic with mesoscopic and continuum level. Such coupling is quite difficult, and no fully satisfactory coupling algorithms have been developed

yet, although significant progress has been made. An alternative method is to embed an MD simulation in a continuum simulation, which we demonstrate in the context of electroosmotic flow in a nanochannel. In the last section we discuss a new method, developed in the late 1990s primarily in Europe: the dissipative particle dynamics (DPD) method. It has features of both LBM and MD algorithms and can be thought of as a coarse-grained version of MD.

In Chapter 17 we turn our attention to simulating full systems across heterogeneous domains, i.e., fluid, thermal, electrical, structural, chemical, etc. To this end, we introduce several reduced-order modeling techniques for analyzing microsystems. Specifically, techniques such as generalized Kirchhoff networks, black box models, and Galerkin methods are described in detail. In black box models, detailed results from simulations are used to construct simplified and more abstract models. Methods such as nonlinear static models and linear and nonlinear dynamic models are described under the framework of black box models. Finally, Galerkin methods, where the basic idea is to create a set of coupled ordinary differential equations, are described. The advantages and limitations of the various techniques are highlighted.

Finally, in Chapter 18 we discuss the application of these techniques to several examples in microflows. First, we present circuit and device models and their application to lab-on-a-chip systems. Then, we discuss reduced-order modeling of squeezed film damping by applying equivalent circuit, Galerkin, mixed-level, and black box models. Next, we present a compact model for electrowetting. Finally, we summarize some of the software packages that are available for reduced-order simulation.

We are very grateful to Prof. Chih-Ming Ho who agreed to provide a foreword to our book. We would like to thank all our colleagues from many different countries who have allowed us to use their work in the previous and this new and expanded edition of the book. We also want to thank Ms. Madeline Brewster at Brown University for her assistance with all aspects of this book, and our students who helped with formatting the figures, especially Vasileios Symeonidis, Pradipkumar Bahukudumbi, and Aveek Chatterjee. AB would like to thank his students I. Ahmed, P. Bahukudumbi, Prof. P. Dutta, Dr. J. Hahm, H.J. Kim, S. Kumar, Dr. J.H. Park, and Prof. C. Sert. The last author (NRA) would like to acknowledge the help of all his students, especially Chatterjee, De, Joseph, and Qiao for letting him use some of the results from their thesis work. NRA is very grateful to Profs. Karniadakis and Beskok for the opportunity to co-author this book with them. NRA would like to thank Profs. Dutton (Stanford), Hess (UIUC), Karniadakis (Brown), Law (Stanford), Pinsky (Stanford), Senturia (MIT), and White (MIT) for mentoring his career.

The first author (GK) would like to thank all members of his family for their support during the course of this effort. The second author (AB) would like to thank Carolyn, Sarah and Sinan for their continuous love,

support and patience. In addition, AB would like to dedicate his work to the memory of his parents, Güngör and Çetin Beşkök. Finally, NRA is deeply indebted to all his family members, especially his parents, Subhas and Krishna Aluru, his brother, Ravi, his wife, Radhika, and his daughter, Neha, for their love, encouragement, and support.

Providence, Rhode Island, USA — George Em Karniadakis
College Station, Texas, USA — Ali Beskok
Urbana, Illinois, USA — Narayan R. Aluru

2

Governing Equations and Slip Models

In this chapter we first present the basic equations of fluid dynamics both for incompressible and compressible flows, and discuss appropriate nondimensionalizations for low-speed and high-speed flows. Although most of the flows encountered in microsystems applications are typically of low speed, micropropulsion applications may involve high-speed supersonic flows (see Section 6.6). Subsequently, we consider the compressible Navier–Stokes equations and develop a general boundary condition for velocity slip. This applies to a regime for which $\mathrm{Kn} < 1$, and it corresponds to a second-order correction in Knudsen number. It improves Maxwell's original first-order formula, which is limited to $\mathrm{Kn} \leq 0.1$. The validity of this model is assessed in Chapter 4 with DSMC data, linearized Boltzmann equation solutions, as well as with experimental results. A more rigorous derivation of the governing equations from the Boltzmann equation is given in Section 15.4.2.

2.1 The Basic Equations of Fluid Dynamics

Consider fluid flow in the nondeformable control volume Ω bounded by the control surface $\partial\Omega$ with $\boldsymbol{n}$ the unit outward normal. The equations of motion can then be derived in an absolute reference frame by applying the principles of mechanics and thermodynamics (Batchelor, 1998). They can be formulated in integral form for mass, momentum, and total energy,

respectively, as

$$\frac{d}{dt}\int_\Omega \rho d\Omega + \int_{\partial\Omega} \rho \boldsymbol{v}\cdot\boldsymbol{n}\, dS = 0, \tag{2.1a}$$

$$\frac{d}{dt}\int_\Omega \rho \boldsymbol{v} d\Omega + \int_{\partial\Omega} [\rho \boldsymbol{v}(\boldsymbol{v}\cdot\boldsymbol{n}) - \boldsymbol{n}\sigma]\, dS = \int_\Omega \boldsymbol{f} d\Omega, \tag{2.1b}$$

$$\frac{d}{dt}\int_\Omega E d\Omega + \int_{\partial\Omega} [E\boldsymbol{v} - \sigma\boldsymbol{v} + \boldsymbol{q}]\cdot\boldsymbol{n}\, dS = \int_\Omega \boldsymbol{f}\cdot\boldsymbol{v} d\Omega. \tag{2.1c}$$

Here $\boldsymbol{v}(\boldsymbol{x},t) = (u,v,w)$ is the velocity field, ρ is the density, and $E = \rho(e + 1/2\boldsymbol{v}\cdot\boldsymbol{v})$ is the total energy, where e represents the internal specific energy. Also, σ is the stress tensor, $\boldsymbol{q}$ is the heat flux vector, and $\boldsymbol{f}$ represents all external forces acting on this control volume. For Newtonian fluids, the stress tensor, which consists of the normal components (p for pressure) and the viscous stress tensor τ, is a *linear* function of the velocity gradient, that is,

$$\sigma = -p\mathbf{I} + \tau, \tag{2.2a}$$

$$\tau = \mu[\nabla\boldsymbol{v} + (\nabla\boldsymbol{v})^T] + \zeta(\nabla\cdot\boldsymbol{v})\mathbf{I}, \tag{2.2b}$$

where $\mathbf{I}$ is the unit tensor, and μ and ζ are the first (absolute) and second (bulk) coefficients of viscosity, respectively. They are related by the Stokes hypothesis, that is, $2\mu + 3\zeta = 0$, which expresses local thermodynamic equilibrium. (We note that the Stokes hypothesis is valid for monoatomic gases but it may not be true in general.) The heat flux vector is related to temperature gradients via the Fourier law of heat conduction, that is,

$$\boldsymbol{q} = -k\nabla T, \tag{2.3}$$

where k is the thermal conductivity, which may be a function of temperature T.

In the case of a *deformable control volume*, the velocity in the flux term should be recognized as in a frame of reference relative to the control surface, and the appropriate time rate of change term should be used. Considering, for example, the mass conservation equation, we have the form

$$\frac{d}{dt}\int_\Omega \rho d\Omega + \int_{\partial\Omega} \rho \boldsymbol{v}_r\cdot\boldsymbol{n}\, dS = 0,$$

or

$$\int_\Omega \frac{\partial\rho}{\partial t}\, d\Omega + \int_{\partial\Omega} \rho\boldsymbol{v}_r\cdot\boldsymbol{n}\, dS + \int_{\partial\Omega} \rho\boldsymbol{v}_{\mathrm{cs}}\cdot\boldsymbol{n}\, dS = 0,$$

where $\boldsymbol{v}_{\mathrm{cs}}$ is the velocity of the control surface, $\boldsymbol{v}_r$ is the velocity of the fluid with respect to the control surface, and the total velocity of the fluid with respect to the chosen frame is $\boldsymbol{v} = \boldsymbol{v}_r + \boldsymbol{v}_{cs}$. The above forms are equivalent, but the first expression may be more useful in applications in which the time history of the volume is of interest.

Equations (2.1a) through (2.1c) can be transformed into an equivalent set of partial differential equations by applying Gauss's theorem (assuming that sufficient conditions of differentiability exist), that is,

$$\frac{\partial \rho}{\partial t} + \nabla\cdot(\rho \boldsymbol{v}) = 0, \tag{2.4a}$$

$$\frac{\partial}{\partial t}(\rho \boldsymbol{v}) + \nabla\cdot[\rho \boldsymbol{v}\boldsymbol{v} - \sigma] = \boldsymbol{f}, \tag{2.4b}$$

$$\frac{\partial}{\partial t}E + \nabla\cdot[E\boldsymbol{v} - \sigma\boldsymbol{v} + \boldsymbol{q}] = \boldsymbol{f}\cdot\boldsymbol{v}. \tag{2.4c}$$

The momentum and energy equations can be rewritten in the following form by using the continuity equation (2.4a) and the constitutive equations (2.2a), (2.2b):

$$\rho\frac{D\boldsymbol{v}}{Dt} = -\nabla p + \nabla\cdot\tau + \boldsymbol{f}, \tag{2.5a}$$

$$\rho\frac{De}{Dt} = -p\nabla\cdot\boldsymbol{v} - \nabla\cdot\boldsymbol{q} + \Phi, \tag{2.5b}$$

where $\Phi = \tau\cdot\nabla\boldsymbol{v}$ is the dissipation function and $D/Dt = \partial/\partial t + \boldsymbol{v}\cdot\nabla$ is the material derivative.

In addition to the governing conservation laws, an equation of state is required. For ideal gases, it has the simple form

$$p = \rho RT, \tag{2.6}$$

where R is the ideal gas constant defined as the difference of the constant specific heats; that is, $R = C_p - C_v$, where $C_v = \frac{\partial e}{\partial T}|_\rho$ and $C_p = \gamma C_v$ with γ the adiabatic index. For ideal gases, the energy equation can be rewritten in terms of the temperature, since $e = p/(\rho(\gamma-1)) = C_vT$, and so equation (2.5b) becomes

$$\rho C_v\frac{DT}{Dt} = -p\nabla\cdot\boldsymbol{v} + \nabla\cdot[k\nabla T] + \Phi. \tag{2.7}$$

The system of equations (2.4a; 2.5a), (2.6), and (2.7) is called *compressible Navier–Stokes equations*, contains six unknown variables $(\rho, \boldsymbol{v}, p, T)$ with six scalar equations. Mathematically, it is an *incomplete parabolic* system, since there are no second-order derivative terms in the continuity equation.

A hyperbolic system arises in the case of inviscid flow, that is, $\mu = 0$ (assuming that we also neglect heat losses by thermal diffusion, that is, $k = 0$). In that case we obtain the *Euler equations*, which in the absence of external forces or heat sources have the form

$$\frac{\partial \rho}{\partial t} + \nabla\cdot(\rho \boldsymbol{v}) = 0, \tag{2.8a}$$

$$\frac{\partial(\rho \boldsymbol{v})}{\partial t} + \nabla\cdot(\rho \boldsymbol{v}\boldsymbol{v}) = -\nabla p, \tag{2.8b}$$

$$\frac{\partial E}{\partial t} + \nabla\cdot[(E+p)\boldsymbol{v}] = 0. \tag{2.8c}$$

This system admits discontinuous solutions, and it can also describe the transition from a supersonic flow (where $|\boldsymbol{v}| > c_s$) to subsonic flow (where $|\boldsymbol{v}| < c_s$), where $c_s = (\gamma RT)^{1/2}$ is the speed of sound. Typically, the transition is obtained through a shock wave, which represents a discontinuity in flow variables. In such a region the integral form of the equations should be used by analogy with equations (2.1a)–(2.1c).

2.1.1 Incompressible Flow

For an incompressible fluid, where $D\rho/Dt = 0$, the mass conservation (or continuity) equation simplifies to

$$\nabla{\cdot}\boldsymbol{v} = 0. \tag{2.9}$$

Typically, when we refer to an incompressible fluid we mean that $\rho =$ constant, but this is not necessary for a divergence-free flow; for example, in thermal convection the density varies with temperature variations. The corresponding momentum equation has the form:

$$\rho\frac{D\boldsymbol{v}}{Dt} = -\nabla p + \nabla{\cdot}\left[\mu[\nabla\boldsymbol{v} + (\nabla\boldsymbol{v})^T]\right] + \boldsymbol{f}, \tag{2.10}$$

where the viscosity $\mu(\boldsymbol{x}, t)$ may vary in space and time. The pressure $p(\boldsymbol{x}, t)$ is not a thermodynamic quantity but can be thought of as a constraint that projects the solution $\boldsymbol{v}(\boldsymbol{x}, t)$ onto a divergence-free space. In other words, an equation of state is no longer valid, since it will make the incompressible Navier–Stokes system overdetermined.

The acceleration terms can be written in various equivalent ways, so that in their discrete form, they conserve total linear momentum $\int_\Omega \rho\boldsymbol{v}\, d\Omega$ and total kinetic energy $\int_\Omega \rho\boldsymbol{v}\cdot\boldsymbol{v}\, d\Omega$ in the absence of viscosity and external forces. In particular, the following forms are often used:

- Convective form: $D\boldsymbol{v}/Dt = \partial\boldsymbol{v}/\partial t + (\boldsymbol{v}\cdot\nabla)\boldsymbol{v}$,
- Conservative (flux) form: $D\boldsymbol{v}/Dt = \partial\boldsymbol{v}/\partial t + \nabla{\cdot}(\boldsymbol{v}\boldsymbol{v})$,
- Rotational form: $D\boldsymbol{v}/Dt = \partial\boldsymbol{v}/\partial t - \boldsymbol{v}\times(\nabla\times\boldsymbol{v}) + 1/2\nabla(\boldsymbol{v}\cdot\boldsymbol{v})$,
- Skew-symmetric form: $D\boldsymbol{v}/Dt = \partial\boldsymbol{v}/\partial t + 1/2[(\boldsymbol{v}\cdot\nabla)\boldsymbol{v} + \nabla{\cdot}(\boldsymbol{v}\boldsymbol{v})]$.

The incompressible Navier–Stokes equations (2.9), (2.10) are written in terms of the primitive variables $(\boldsymbol{v}, p)$. An alternative form is to rewrite these equations in terms of the velocity $\boldsymbol{v}$ and vorticity $\omega = \nabla\times\boldsymbol{v}$. This is a more general formulation than the standard vorticity-streamfunction, which is limited to two dimensions. The following system is equivalent to

equations (2.10) and (2.9), assuming that ρ, μ are constant:

$$\rho \frac{D\omega}{Dt} = (\omega \cdot \nabla)\boldsymbol{v} + \mu \nabla^2 \omega \quad \text{in} \quad \Omega, \tag{2.11a}$$

$$\nabla^2 \boldsymbol{v} = -\nabla \times \omega \quad \text{in} \quad \Omega, \tag{2.11b}$$

$$\nabla \cdot \boldsymbol{v} = 0 \quad \text{in} \quad \Omega, \tag{2.11c}$$

$$\omega = \nabla \times \boldsymbol{v} \quad \text{in} \quad \Omega, \tag{2.11d}$$

where the elliptic equation for the velocity $\boldsymbol{v}$ is obtained using a vector identity and the divergence-free constraint. We also assume here that the domain Ω is simply connected. An equivalent system in terms of velocity and vorticity is studied in (Karniadakis and Sherwin, 1999). The problem with the lack of direct boundary conditions for the vorticity also exists in the more often used vorticity-streamfunction formulation in two dimensions.

Finally, a note regarding **nondimensionalization**. Consider the free-stream flow U_0 past a body of characteristic size D in a medium of dynamic viscosity μ as shown in Figure 2.1. There are two characteristic time scales in the problem, the first one representing the *convective time scale* $t_c = D/U_0$, and the second one representing the *diffusive time scale* $t_d = D^2/\nu$, where $\nu = \mu/\rho$ is the kinematic viscosity. If we nondimensionalize all lengths with D, the velocity field with U_0, and the vorticity field with U_0/D, we obtain two different nondimensional equations corresponding to the choice of the time nondimensionalization:

Incompressible High-Speed Flows:

$$\frac{\partial \omega}{\partial t_c^*} + \nabla \cdot (\boldsymbol{v}\omega) = (\omega \cdot \nabla)\boldsymbol{v} + Re^{-1} \nabla^2 \omega,$$

Incompressible Low-Speed Flows:

$$\frac{\partial \omega}{\partial t_d *} + \mathrm{Re} \nabla \cdot (\boldsymbol{v}\omega) = \mathrm{Re}(\omega \cdot \nabla)\boldsymbol{v} + \nabla^2 \omega,$$

where t_c^* and t_d^* are the nondimensionalized time variables with respect to t_c and t_d, respectively, and $\mathrm{Re} = U_0 D/\nu$ is the Reynolds number. Both forms are useful in simulations, the first in high Reynolds number simulations (e.g., micronozzles, Section 6.6), and the second in low Reynolds number flows (e.g., microchannels).

In many microflow problems the nonlinear terms can be neglected, and in such cases the governing equations are the **Stokes equations**, which we can cast in the form

$$-\nu \nabla^2 \boldsymbol{v} + \nabla p/\rho = \boldsymbol{f} \quad \text{in} \quad \Omega, \tag{2.12a}$$

$$\nabla \cdot \boldsymbol{v} = 0 \quad \text{in} \quad \Omega, \tag{2.12b}$$

along with appropriate boundary conditions for $\boldsymbol{v}$.

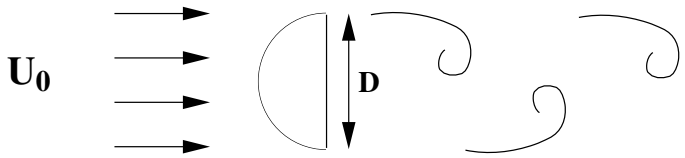

FIGURE 2.1. A schematic of free-stream flow past a microprobe in a viscous fluid.

2.1.2 Reduced Models

The mathematical nature of the Navier–Stokes equations varies depending on the flow that we model and the corresponding terms that dominate in the equations. For example, for an inviscid compressible flow, we obtain the Euler equations, which are of hyperbolic nature, whereas the incompressible Euler equations are of hybrid type corresponding to both real and imaginary eigenvalues. The unsteady incompressible Navier–Stokes equations are of mixed parabolic/hyperbolic nature, but the steady incompressible Navier–Stokes equations are of elliptic/parabolic type. It is instructive, especially for a reader with not much experience in fluid mechanics, to follow a hierarchical approach in reducing the Navier–Stokes equations to simpler equations so that each introduces one new concept.

Taking as an example the incompressible Navier–Stokes equations (2.9), (2.10), a simpler model is the *unsteady Stokes* system. This retains all the complexity but not the nonlinear terms; that is,

$$\begin{aligned} \frac{\partial \boldsymbol{v}}{\partial t} &= -\nabla p/\rho + \nu \nabla^2 \boldsymbol{v} + \boldsymbol{f} \\ \nabla \cdot \boldsymbol{v} &= 0. \end{aligned}$$

The Stokes system [equations (2.12a) and (2.12b)] is recovered by dropping the time derivative. Alternatively, we can drop the divergence-free constraint and study the purely parabolic scalar equation for a variable u, that is,

$$\frac{\partial u}{\partial t} = \nu \nabla^2 u + f. \tag{2.13}$$

This equation expresses unsteady diffusion and includes volumetric source terms. If we instead drop all terms on the right-hand side of (2.10), as well as the divergence-free constraint, we obtain a nonlinear advection equation. Finally, by dropping the time derivative in the parabolic equation (2.13), we obtain the **Poisson equation**,

$$-\nu \nabla^2 u = f,$$

which is encountered often in MEMS (micro electro mechanical systems), e.g., in electrostatics.

2.2 Compressible Flow

The flow regime for Kn < 0.01 is known as the *continuum regime*, where the Navier–Stokes equations with no-slip boundary conditions govern the flow. In the *slip flow regime* ($0.01 \leq$ Kn ≤ 0.1) the often-assumed no-slip boundary conditions seem to fail, and a sublayer on the order of one mean free path, known as the Knudsen layer, starts to become dominant between the bulk of the fluid and the wall surface. The flow, in the Knudsen layer cannot be analyzed with the Navier–Stokes equations, and it requires special solutions of the Boltzmann equation (see Section 15.4 and also (Sone, 2002)). However, for Kn ≤ 0.1, the Knudsen layer covers less than 10% of the channel height (or the boundary layer thickness for external flows), and this layer can be neglected by extrapolating the bulk gas flow towards the walls. This results in a finite velocity slip value at the wall, and the corresponding flow regime is known as the *slip flow regime* (i.e., $0.01 \leq$ Kn ≤ 0.1). In the slip flow regime the flow is governed by the Navier–Stokes equations, and rarefaction effects are modeled through the partial slip at the wall using Maxwell's velocity slip and von Smoluchowski's temperature jump boundary conditions (Kennard, 1938).

> For example, it may, however, be misleading to identify the flow regimes as "slip" and "continuum," since the "no-slip" boundary condition is just an empirical finding, and the Navier-Stokes equations are valid for both the slip and the continuum flow regimes. Nevertheless, this identification was first made for rarefied gas flow research almost a century ago, and we will follow this terminology throughout this book.

In the *transition regime* (Kn ≥ 0.1) the constitutive laws that define the stress tensor and the heat flux vector break down (Chapman and Cowling, 1970), requiring higher-order corrections to the constitutive laws, resulting in the Burnett or Woods equations (Woods, 1993). It is also possible to use the Boltzmann equation directly, which is valid at the microscopic level (see Section 15.4). The Burnett and Woods equations are derived from the Boltzmann equation based on the Chapman–Enskog expansion of the velocity distribution function f, including terms up to Kn^2 in the following form:

$$f = f_0(1 + a\,\mathrm{Kn} + b\,\mathrm{Kn}^2), \tag{2.14}$$

where a and b are functions of gas density, temperature, and macroscopic velocity vector, and f_o is the equilibrium (Maxwellian) distribution function (Chapman and Cowling, 1970):

$$f_0 = \left(\frac{m}{2\pi k_B T_0}\right)^{3/2} \exp\left(-\frac{mv^2}{2k_B T_0}\right), \tag{2.15}$$

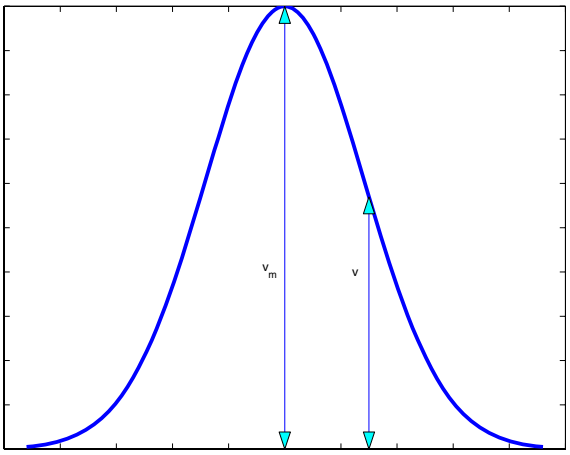

FIGURE 2.2. A plot of the Maxwellian distribution showing the most probable velocity and the mean thermal velocity, equation (2.15).

which is plotted in Figure 2.2. Here m is the molecular mass, k_{B} is the Boltzmann constant, T_0 is the temperature, and v is the mean thermal velocity of the molecules. The zeroth–order solution of equation (2.14) is the equilibrium solution, where flow gradients vanish; i.e., the viscous stress tensor and the heat flux vector vanish, giving the Euler equations (Chapman and Cowling, 1970). Therefore, $\mathrm{Kn} \equiv 0$ corresponds to the Euler equations. This is a *singular limit* in transition from the Navier–Stokes equations to the Euler equations, where the infinitesimally small viscosity (or heat conduction coefficient) vanishes.

Remark: In this book $\mathrm{Kn} = 0$ is commonly used to indicate the *no-slip* flow limit, and hence in the rest of this work $\mathrm{Kn} = 0$ indicates a limit that $\mathrm{Kn} \to 0$, but never $\mathrm{Kn} \equiv 0$!

The first-order solution in Kn yields the Navier–Stokes equations, and the second-order solution in Kn yields the Burnett equations. The Woods equations have a different form in the high-order corrections of the stress tensor and heat flux terms (Woods, 1993; Welder et al., 1993).

We rewrite here equations (2.4b), (2.4c) for compressible flows in two dimensions:

$$\frac{\partial}{\partial t}\begin{pmatrix}\rho\\ \rho u_1\\ \rho u_2\\ E\end{pmatrix}+\frac{\partial}{\partial x_1}\begin{pmatrix}\rho u_1\\ \rho u_1^2+p+\sigma_{11}\\ \rho u_1 u_2+\sigma_{12}\\ (E+p+\sigma_{11})\cdot u_1+\sigma_{12}\cdot u_2+q_1\end{pmatrix}$$
$$+\frac{\partial}{\partial x_2}\begin{pmatrix}\rho u_2\\ \rho u_1 u_2+\sigma_{21}\\ \rho u_2^2+p+\sigma_{22}\\ (E+p+\sigma_{22})\cdot u_2+\sigma_{21}\cdot u_1+q_2\end{pmatrix}=0, \quad (2.16)$$

where the two velocity components are denoted by $(u_1, u_2) \equiv (u, v)$ in the Cartesian coordinate system $(x_1, x_2) \equiv (x, y)$.

Remark: The conservation equations (2.16) are valid for continuum as well as for rarefied flows. However, the viscous stresses (σ_{ij}) and the heat flux (q_i) have to be determined differently for different flow regimes (see ection 15.4.2). Specifically, the *thermal stresses*

$$\frac{\partial^2 T}{\partial x_i \partial x_j}-\frac{1}{3}\frac{\partial^2 T}{\partial x_k^2}\delta_{ij}$$

in the momentum equation (derived from the Boltzmann equation) are not included in the Newtonian law for fluids. Similarly, the term in the energy equation

$$\frac{\partial^2 u_i}{\partial x_j^2}$$

is not present in the Fourier law. These terms are derived in the asymptotic analysis of the Boltzmann equation in the limit of small deviation from equilibrium (Sone, 2002). For small Knudsen number flows and with $\mathcal{O}(M) \sim \mathcal{O}(\mathrm{Kn})$, the thermal stress in the momentum equation can be absorbed in the pressure term. However, if the Reynolds number of the system is large or the temperature variation is not small, then the thermal stress cannot be included in the pressure term. In this case, these extra terms have to be included explicitly in the governing equations, which are different from the above compressible Navier–Stokes equations (Sone, 2002). To this end, also the work of (Myong, 1998) may be consulted. He derived thermodynamically consistent hydrodynamic models for high Knudsen number gas flows, valid uniformly for all Mach number flows and satisfying the second law of thermodynamics.

2.2.1 First-Order Models

By first-order models we refer to the approximation of the Boltzmann equation up to $\mathcal{O}(Kn)$, i.e., the compressible Navier-Stokes equations. The con-

stitutive laws from equations (2.2a) and (2.2b) are

$$\sigma_{ij}^{NS} = -\mu\left(\frac{\partial u_j}{\partial x_i} + \frac{\partial u_i}{\partial x_j}\right) + \mu\frac{2}{3}\frac{\partial u_m}{\partial x_m}\delta_{ij} - \zeta\frac{\partial u_m}{\partial x_m}\delta_{ij}, \tag{2.17}$$

where μ and ζ are the dynamic (first coefficient)) and bulk (second coefficient) viscosities of the fluid, and δ_{ij} is the Kronecker delta. The heat flux is determined from Fourier's law (equation (2.3)). This level of conservation equations defines the *compressible Navier–Stokes equations*.

In the *slip flow* regime, the Navier–Stokes equations (2.16), (2.17) are solved subject to the velocity slip and temperature jump boundary conditions given by

$$u_s - u_w = \frac{2-\sigma_v}{\sigma_v}\frac{1}{\rho(2RT_w/\pi)^{1/2}}\tau_s + \frac{3}{4}\frac{\Pr(\gamma-1)}{\gamma\rho RT_w}(-q_s), \tag{2.18}$$

$$T_s - T_w = \frac{2-\sigma_T}{\sigma_T}\left[\frac{2(\gamma-1)}{\gamma+1}\right]\frac{1}{R\rho(2RT_w/\pi)^{1/2}}(-q_n), \tag{2.19}$$

where q_n, q_s are the normal and tangential heat flux components to the wall. Also, τ_s is the viscous stress component corresponding to the skin friction, γ is the ratio of specific heats, u_w and T_w are the reference wall velocity and temperature, respectively. Here Pr is the Prandtl number

$$\Pr = \frac{C_p\mu}{k}.$$

Equation (2.19) was proposed by Maxwell in 1879. The second term in (2.19) is associated with the thermal creep (transpiration) phenomenon, which can be important in causing pressure variation along channels in the presence of tangential temperature gradients (see Section 5.1). Since the fluid motion in a rarefied gas can be started with tangential temperature variations along the surface, the momentum and energy equations are coupled through the thermal creep effects. In addition, there are other thermal stress terms that are omitted in classical gas dynamics, but they may be present in rarefied microflows, as we discuss in Section 5.1. Equation (2.19) is due to von Smoluchowski (Kennard, 1938); it models temperature jump effects. Here σ_v, σ_T **are the tangential momentum and energy accommodation coefficients**, respectively (see Section 2.2.2). After nondimensionalization with a reference velocity and temperature, the slip conditions are written as follows:

$$U_s - U_w = \frac{2-\sigma_v}{\sigma_v}\,\mathrm{Kn}\,\frac{\partial U_s}{\partial n} + \frac{3}{2\pi}\frac{(\gamma-1)}{\gamma}\frac{\mathrm{Kn}^2\,\mathrm{Re}}{\mathrm{Ec}}\frac{\partial T}{\partial s}, \tag{2.20a}$$

$$T_s - T_w = \frac{2-\sigma_T}{\sigma_T}\left[\frac{2\gamma}{\gamma+1}\right]\frac{\mathrm{Kn}}{\Pr}\frac{\partial T}{\partial n}, \tag{2.20b}$$

where the capital letters are used to indicate nondimensional quantities. Also, **n** and **s** denote the outward normal (unit) vector and the tangential (unit) vector.

Remark: Note that while the second term on the right-hand side of equation (2.20b) (thermal creep effect) appears to be $\mathcal{O}(\mathrm{Kn}^2)$, it actually corresponds to a first-order expansion (in Kn) of the Boltzmann equation. So both velocity jump and thermal creep are derived from an $\mathcal{O}(\mathrm{Kn})$ asymptotic expansion of the Boltzmann equation (Sone, 2002).

To determine fully the momentum and energy transport in microdomains, we need the following nondimensional numbers:

- *Reynolds number:* $\mathrm{Re} = \frac{\rho u h}{\mu}$,
- *Eckert number:* $\mathrm{Ec} = \frac{u^2}{C_p \Delta T}$, and
- *Knudsen number:* $\mathrm{Kn} = \frac{\lambda}{h}$.

However, it is possible to introduce a functional relation for Knudsen number and Eckert number in terms of the Mach number

$$M = \frac{u}{\sqrt{\gamma R T_0}}.$$

The Knudsen number can be written in terms of the Mach number and Reynolds number as

$$\mathrm{Kn} = \frac{\mu}{h\rho(2RT_w/\pi)^{1/2}} = \sqrt{\pi\gamma/2}\frac{M}{\mathrm{Re}}, \tag{2.21}$$

while the Eckert number can be written as

$$\mathrm{Ec} = (\gamma - 1)\frac{T_0}{\Delta T}M^2, \tag{2.22}$$

where ΔT is a specified temperature difference in the domain, and T_0 is the reference temperature used to define the Mach number. Using these relations for Ec and M, the independent parameters of the problem are reduced to three:

- **Prandtl number Pr, Reynolds number Re, and Knudsen number Kn**.

2.2.2 The Role of the Accommodation Coefficients

Momentum and energy transfer between the gas molecules and the surface requires specification of interactions between the impinging gas molecules and the surface. A detailed analysis of this is quite complicated and requires complete knowledge of the scattering kernels (see Section 15.4). From the

macroscopic viewpoint, it is sufficient to know some average parameters in terms of the so-called momentum and thermal accommodation coefficients in order to describe gas–wall interactions. The **thermal accommodation coefficient** (σ_T) is defined by

$$\sigma_T = \frac{dE_i - dE_r}{dE_i - dE_w}, \tag{2.23}$$

where dE_i and dE_r denote the energy fluxes of incoming and reflected molecules per unit time, respectively, and dE_w denotes the energy flux if all the incoming molecules had been reemitted with the energy flux corresponding to the surface temperature T_w. The perfect energy exchange case corresponds to $\sigma_T = 1$. A separate thermal accommodation coefficient can be defined for the effects of gas–surface interactions on transitional, rotational, and vibrational energies of the molecules. Experimental evidence indicates that under such interactions the transitional and rotational energy components are more affected compared to the vibrational energy of the molecules (Schaaf and Chambre, 1961). However, such refinements cannot be applied to macroscopic models, since the rarefaction effects are treated by solving the continuum energy equation with the temperature jump boundary condition. DSMC models (see Section 15.1) can be more flexible in employing various molecule–wall collision models for different modes of energy transfer, as we show in Section 15.4.

The **tangential momentum accommodation coefficient** (σ_v) can be defined for tangential momentum exchange of gas molecules with surfaces

$$\sigma_v = \frac{\tau_i - \tau_r}{\tau_i - \tau_w}, \tag{2.24}$$

where τ_i and τ_r show the tangential momentum of incoming and reflected molecules, respectively, and τ_w is the tangential momentum of reemitted molecules, corresponding to that of the surface ($\tau_w = 0$ for stationary surfaces).

- The case of $\sigma_v = 0$ is called **specular reflection**,

where the tangential velocity of the molecules reflected from the walls is unchanged, but the normal velocity of the molecules is reversed due to the normal momentum transfer to the wall. In this case there is no tangential momentum exchange of fluid with the wall, resulting in zero skin friction. This is a limit of *inviscid flow*, where viscous stresses are zero. Hence

$$\frac{\partial u_s}{\partial n} \to 0 \quad \text{as} \quad \sigma_v \to 0,$$

and equation (2.20b) becomes obsolete, since the Euler equations require only the no-penetration boundary condition in this limit.

- The case of $\sigma_v = 1$ is called **diffuse reflection**.

TABLE 2.1. Thermal and tangential momentum accommodation coefficients for typical gases and surfaces (Seidl and Steinheil, 1974; Lord, 1976).

Gas	Surface	σ_T	σ_v
Air	Al	0.87–0.97	0.87–0.97
He	Al	0.073	
Air	Iron	0.87–0.96	0.87–0.93
H_2	Iron	0.31–0.55	
Air	Bronze		0.88–0.95

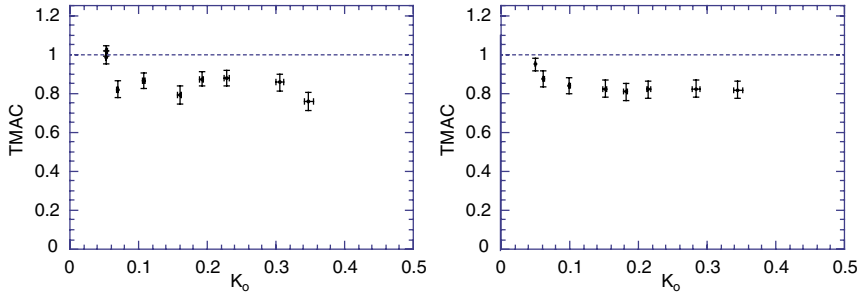

FIGURE 2.3. Tangential momentum accommodation coefficient σ_v (TMAC) versus Knudsen number obtained from mass flowrate measurements for argon (left) and for nitrogen (right). (Courtesy of K. Breuer.)

In this case the molecules are reflected from the walls with zero average tangential velocity. Therefore, the diffuse reflection is an important case for tangential momentum exchange (and thus friction) of the gas with the walls.

The tangential momentum and thermal accommodation coefficients depend on the gas and surface temperatures, local pressure, and possibly the velocity and the mean direction of the local flow. They are usually tabulated for some common gases and surfaces; see Table 2.1 and for details (Seidl and Steinheil, 1974; Lord, 1976). Diffuse reflection is likely to occur for rough surfaces. The values of σ_v and σ_T are not necessarily equal, as shown in Table 2.1. Typically, it takes a few surface collisions for a molecule to adopt the average tangential momentum of the surface, but it takes more surface collisions to obtain the energy level of the surface. Under laboratory conditions, values as low as 0.2 have been observed (Lord, 1976). Very low values of σ_v will increase the slip on the walls considerably even for small Knudsen number flows due to the $(2-\sigma)/\sigma$ factor multiplying the velocity slip and temperature jump equations.

Measurements or direct computation of accommodation coefficients are very difficult to obtain. The accommodation coefficients for microchannel flows were measured indirectly using the first-order (Arkilic et al., 2001)

and second-order slip flow theories (Maurer et al., 2003; Colin et al., 2004). Measurements of accommodation coefficients in (Arkilic et al., 2001) were obtained in the microchannel described in Chapter 1 (see Figure 1.18). Using high-resolution measurements for the mass flowrate and plotting it against the inverse pressure, the slope was computed, and based on the slip theory equations (see Chapter 4), the tangential momentum accommodation coefficient (TMAC) was obtained. The results of such measurements for argon and nitrogen are plotted in Figure 2.3 as a function of the Knudsen number. The measured value is $\sigma_v \approx 0.80$ for nitrogen or argon or carbon dioxide in contact with prime silicon crystal in the slip and early transitional flow regime ($0 < \mathrm{Kn} \leq 0.4$). It is observed that σ_v is less than unity, and independent of Kn in that range (Arkilic, 1997; Arkilic et al., 2001). Lower accommodation coefficients are possible due to the low surface roughness of prime silicon crystal.

(Maurer et al., 2003) presented experimental results for helium and nitrogen flow in 1.14 μm deep 200 μm wide glass channel covered by an atomically flat silicon surface. Flow behavior in the slip and early transition regimes was investigated for channel-averaged Knudsen numbers of 0.8 and 0.6 for helium and nitrogen flows, respectively. Using the flowrate data and a second-order slip model represented by equation (2.42), TMAC values of 0.91 ± 0.03 for helium, and 0.87 ± 0.06 for nitrogen were obtained. The authors also estimated the upper limit of slip flow regime as $\mathrm{Kn} = 0.3 \pm 0.1$, where Kn is based on the channel height. In a separate study, (Colin et al., 2004) presented experimental results for nitrogen and helium flow in a series of silicon microchannels fabricated using deep reactive ion etching (DRIE). Using mass flowrate and the corresponding pressure drop data, and the second-order slip model by (Deissler, 1964), they reported TMAC values of 0.93 for both helium and nitrogen. These authors reported breakdown of the first-order slip model for $\mathrm{Kn} \geq 0.05$, and of the second-order theory of Deissler for $\mathrm{Kn} \geq 0.25$, where Kn was based on the channel depth. These limits are unusually low compared to the values commonly accepted in the literature. A comparison between the experiments of (Colin et al., 2004) and (Maurer et al., 2003) shows that the uncertainty in the channel depth was ± 0.1 μm for Colin's channels, where it was 0.02 μm for Maurer's channels. In addition, the fabrication methods and the channel aspect ratios in these studies were different. These are certainly some of the reasons for the differences between the measurements of TMAC values by these two groups.

Finally, we note that

- *It is possible to predict the (pressure–driven) channel flowrate in the early transition flow regime, using a second–order slip solution of the Navier–Stokes equations. However, this procedure may create erroneous velocity profiles*, as shown in Figures 4.11 and 4.17.

We caution the reader about these limitations of the second-order theory

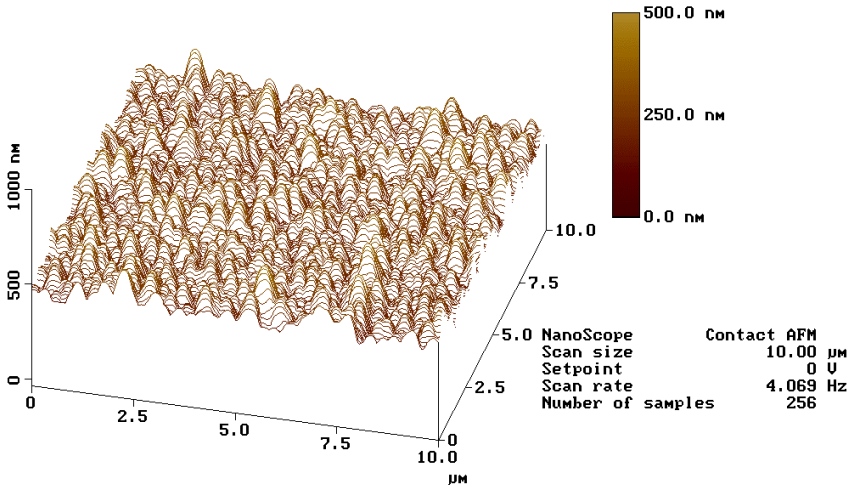

FIGURE 2.4. Profile of a polysilicon mirror surface; scan area 10×10 μm. (Courtesy of C. Liu.)

in the context of validation efforts using integral (e.g., mass flowrate versus pressure drop) measurements.

Roughness plays a very important role in microscales, but it is difficult to quantify its effect. In practice, it can be characterized using an atomic force microscope (AFM) for nonconductive surfaces, scanning tunnelling microscope (STM) for conductive surfaces, WYCO interferometer for optical nondestructive evaluation, and scanning electron microscope (SEM). Micron–scale roughness can be produced by wet chemical etching. A typical surface profile for a polysilicon mirror surface is shown in Figure 2.4.

The effects of roughness are difficult to analyze theoretically or numerically, but some progress has been made. (Richardson, 1973) considered a periodically modulated (rough) wall and applied a shear stress-free boundary condition. He showed analytically that the no-slip boundary condition is actually a consequence of surface roughness. In a systematic molecular dynamics study, (Mo and Rosenberger, 1990) investigated the effects of both periodic and random roughness with amplitude A. They found that as the roughness height (amplitude) A increases compared to the mean free path λ, the velocity slip at the wall decreases. Specifically, they proposed a criterion for the no-slip condition to be valid based on the ratio λ/A. If this ratio is of order unity, that is, if the roughness height is smaller but comparable to the mean free path, then the no-slip condition is satisfied. Otherwise, significant slip at the wall is present, which for atomically smooth walls occurs if the global Knudsen number, i.e., the ratio λ/h (with h the channel height), is finite. In summary, it was concluded that:

- For a microchannel flow with atomically **smooth** walls, if the global Knudsen number $\mathrm{Kn}_g = \lambda/h$ is less than 0.01, then the no-slip condition at the walls is valid (h is the channel height).
- For a microchannel flow with atomically **rough** walls, if the local Knudsen number $\mathrm{Kn}_l = \lambda/A$ is of order unity, then the no-slip condition at the walls is valid (A is the roughness height).
- Otherwise, in both smooth or rough walls, there is significant velocity slip at the walls.

In another study, (Li et al., 2002) considered surface roughness effects on gas flows through long microtubes. They treated the rough surface as a porous film covering an impermeable surface. In the porous film region they used the Brinkman-extended Darcy model, and they employed a high-order slip model in the core region of the microtubes. Solutions in these two different regions of the tube were combined by matching the velocity slip and the shear stress at the porous-core flow interface. This enabled derivation of expressions for the pressure distribution in microtubes, including the slip effects.

2.3 High-Order Models

The conservation equations (2.16) are still valid for larger deviations from the equilibrium conditions; however, the stress tensor (and heat flux vector) have to be corrected for high-order rarefaction effects. The general tensor expression of the Burnett level stress tensor is

$$\begin{aligned}\sigma_{ij}^B = -2\mu\overline{\frac{\partial u_i}{\partial x_j}} + \frac{\mu^2}{p}\Bigg[&\omega_1\frac{\partial u_k}{\partial x_k}\overline{\frac{\partial u_i}{\partial x_j}} + \omega_2\left(\frac{D}{Dt}\overline{\frac{\partial u_i}{\partial x_j}} - 2\overline{\overline{\frac{\partial u_i}{\partial x_k}}\frac{\partial u_k}{\partial x_j}}\right)\\ &+ \omega_3 R\overline{\frac{\partial^2 T}{\partial x_i \partial x_j}} + \omega_4\frac{1}{\rho T}\overline{\frac{\partial p}{\partial x_i}\frac{\partial T}{\partial x_j}} + \omega_5\frac{R}{T}\overline{\frac{\partial T}{\partial x_i}\frac{\partial T}{\partial x_j}}\\ &+ \omega_6\overline{\overline{\frac{\partial u_i}{\partial x_k}}\overline{\frac{\partial u_k}{\partial x_j}}}\Bigg],\end{aligned} \tag{2.25}$$

where a bar over a tensor designates a nondivergent symmetric tensor, i.e.,

$$\overline{f_{ij}} = (f_{ij} + f_{ji})/2 - \delta_{ij}/3 f_{mm}.$$

Similar expressions are valid for the heat flux q_i^B (Zhong, 1993). The coefficients ω_i depend on the gas model and have been tabulated for hard spheres and Maxwellian gas models (Schamberg, 1947; Zhong, 1993). Since the Burnett equations are of second order in Kn, they are valid in the early transition flow regime. However, fine-grid numerical solutions of certain

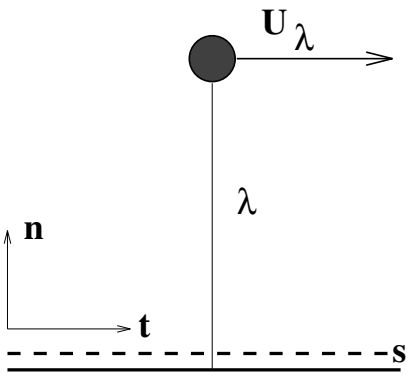

FIGURE 2.5. Control surface for tangential momentum flux near an isothermal wall moving at velocity U_w.

versions of the Burnett equations result in small wavelength instabilities. The cause of this instability has been traced to violation of the second law of thermodynamics (Balakrishnan, 2004). Using the Chapman–Enskog expansion and the Bhatnagar–Gross–Krook model of the collision integral, Balakrishnan (2004) derived the BGK–Burnett equations, and reported that the entropy-consistent behavior of the BGK–Burnett equations depends on the moment closure coefficients and approximations of the total derivative terms ($\frac{D}{Dt}$) in equation (2.25). In the following we use the exact definition of the total derivative instead of the Euler approximation most commonly used in hypersonic rarefied flows (Zhong, 1993). Numerical solutions of the Burnett equations for sevearal gas microflows can be found in (Agarwal et al., 2001; Agarwal and Yun, 2002; Xu, 2003; Lockerby and Reese, 2003; Xue et al., 2003).

Since the Burnett equations are obtained by a second-order Chapman–Enskog expansion in Kn, they require second-order slip boundary conditions. Such boundary conditions were derived by (Schamberg, 1947); however, numerical experiments with aerodynamic rarefied flows (Zhong, 1993) showed that Schamberg's boundary conditions are inaccurate for $\mathrm{Kn} > 0.2$. Similar second-order slip boundary conditions have also been proposed in (Deissler, 1964) and (Sreekanth, 1969). Detailed discussions of performance of these second-order slip models will be presented in Sections 4.1.3 and 4.2, with comparisons of the DSMC and the linearized Boltzmann results against the analytical predictions for the velocity profile.

2.3.1 Derivation of High-Order Slip Models

Maxwell's derivation of equation (2.19) is based on kinetic theory. A similar boundary condition can be derived by an approximate analysis of the motion of gas in isothermal conditions. We write the tangential momentum

flux on a surface s located near the wall (see Figure 2.5) as

$$\frac{1}{4}n_s m\bar{v}u_s,$$

where n_s is the number density of the molecules crossing surface s, m is the molecular mass, $\bar{v}$ is the mean thermal speed defined as

$$\bar{v} = (8/\pi RT)^{0.5},$$

and u_s is the tangential (slip) velocity of the gas on this surface. If we assume that approximately half of the molecules passing through s are coming from a layer of gas at a distance proportional to one mean free path ($\lambda = [\mu(RT\pi/2)^{\frac{1}{2}}/p]$) away from the surface, the tangential momentum flux of these incoming molecules is written as

$$\frac{1}{4}n_\lambda m\bar{v}_\lambda u_\lambda,$$

where the subscript λ indicates quantities evaluated one mean free path away from the surface. Since we have assumed that half of the molecules passing through s are coming from λ away from this surface $n_\lambda = \frac{1}{2}n_s$, the other half of the molecules passing through s are reflected from the wall (see Figure 2.5), and they bring to surface s a tangential momentum flux of

$$\frac{1}{4}n_w m\bar{v}_w u_r,$$

where the subscript w indicates wall conditions and the number density n_w is equal to $\frac{1}{2}n_s$. The average tangential velocity of the molecules reflected from the wall is shown by u_r. For determination of u_r we will use the definition of tangential momentum accommodation coefficient σ_v. Assuming that σ_v (in percentage) of the molecules are reflected from the wall *diffusely* (i.e., with average tangential velocity corresponding to that of the wall u_w), and $(1 - \sigma_v)$ (in percentage) of the molecules are reflected from the wall *specularly* (i.e., conserving their average incoming tangential velocity u_λ), we have

$$u_r = (1 - \sigma_v)u_\lambda + \sigma_v u_w.$$

Therefore, the total tangential momentum flux on surface s is written as

$$\frac{1}{4}n_s m\bar{v}u_s = \frac{1}{4}n_\lambda m\bar{v}_\lambda u_\lambda + \frac{1}{4}n_w m\bar{v}_w\left[(1 - \sigma_v)u_\lambda + \sigma_v u_w\right].$$

Since we have assumed that the temperatures of the fluid and the surface are the same, the mean thermal speeds are identical (i.e., $\bar{v}_s = \bar{v}_\lambda = \bar{v}_w$); this is a rather strong assumption in our derivation. The number density

n_s of molecules passing through the surface is composed of n_λ and n_w. We have assumed that $n_\lambda = n_w = \frac{1}{2}n_s$, which is approximately true if there is no accumulation or condensation of gas on the surface. Using the tangential momentum flux relation, the mean tangential velocity of the gas molecules on the surface, called **slip velocity**, is

$$u_s = \frac{1}{2}[u_\lambda + (1-\sigma_v)u_\lambda + \sigma_v u_w]. \tag{2.26}$$

Schaaf and Chambre (1961) have written this expression as an average tangential velocity on a surface adjacent to an isothermal wall. Our derivation results in the same relation with approximately similar assumptions. Notice that instead of obtaining the slip information u_λ one mean free path away from the wall, a fraction of λ may be used; see (Thompson and Owens, 1975). Using a Taylor series expansion for u_λ about u_s, we obtain

$$\begin{aligned} u_s = {} & \frac{1}{2}\left[u_s + \lambda\left(\frac{\partial u}{\partial n}\right)_s + \frac{\lambda^2}{2}\left(\frac{\partial^2 u}{\partial n^2}\right)_s + \cdots\right] \\ & + \frac{1}{2}\left\{(1-\sigma_v)\left[u_s + \lambda\left(\frac{\partial u}{\partial n}\right)_s + \frac{\lambda^2}{2}\left(\frac{\partial^2 u}{\partial n^2}\right)_s + \cdots\right] + \sigma_v \cdot u_w\right\}, \end{aligned}$$

where the normal coordinate to the wall is denoted by n. This expansion results in the following slip relation on the boundaries:

$$u_s - u_w = \frac{2-\sigma_v}{\sigma_v}\left[\lambda\left(\frac{\partial u}{\partial n}\right)_s + \frac{\lambda^2}{2}\left(\frac{\partial^2 u}{\partial n^2}\right)_s + \cdots\right]. \tag{2.27}$$

After nondimensionalization with a reference length and velocity scale (such as free-stream velocity), we obtain

$$U_s - U_w = \frac{2-\sigma_v}{\sigma_v}\left[\mathrm{Kn}\left(\frac{\partial U}{\partial n}\right)_s + \frac{\mathrm{Kn}^2}{2}\left(\frac{\partial^2 U}{\partial n^2}\right)_s + \cdots\right], \tag{2.28}$$

where we have denoted the nondimensional quantities with capital letters. By neglecting the higher-order terms in the above equation we recover Maxwell's first-order slip boundary condition (2.19) in nondimensional form. Similarly, if we truncate the above equation to include only up to second-order terms in Kn, we obtain

$$U_s - U_w = \frac{2-\sigma_v}{\sigma_v}\left[\mathrm{Kn}\left(\frac{\partial U}{\partial n}\right)_s + \frac{\mathrm{Kn}^2}{2}\left(\frac{\partial^2 U}{\partial n^2}\right)_s\right]. \tag{2.29}$$

We will use this equation for comparison of various slip models in Section 2.3.3 and in Section 4.2 .

Equation (2.26) excludes the thermal creep terms of equation (2.19), since isothermal conditions are assumed in its derivation. For nonisothermal

flows, the thermal creep effects are included to equation (2.26) separately, resulting in the following relation:

$$u_s = \frac{1}{2}[u_\lambda + (1-\sigma_v)u_\lambda + \sigma_v u_w] + \frac{3}{4}\frac{\Pr(\gamma-1)}{\gamma\rho R T_w}(-q_s).$$

For the temperature jump boundary condition, a derivation based on the kinetic theory of gases is given in (Kennard, 1938). We propose the following form for the high-order temperature jump condition by analogy with equation (2.28):

$$T_s - T_w = \frac{2-\sigma_T}{\sigma_T}\left[\frac{2\gamma}{\gamma+1}\right]\frac{1}{Pr}\left[Kn\left(\frac{\partial T}{\partial n}\right)_s + \frac{Kn^2}{2}\left(\frac{\partial^2 T}{\partial n^2}\right)_s + \frac{\mathrm{Kn}^3}{6}\left(\frac{\partial^3 T}{\partial n^3}\right)_s + \cdots\right], \tag{2.30}$$

which can be rearranged by recognizing the Taylor series expansion of T_λ about T_s to give a bf temperature jump boundary condition similar to equation (2.26) as

$$T_s = \left(\frac{(2-\sigma_T)}{\Pr}\frac{2\gamma}{(\gamma+1)}T_\lambda + \sigma_T T_w\right) \Big/ \left(\sigma_T + \frac{2\gamma}{(\gamma+1)}\frac{(2-\sigma_T)}{\Pr}\right). \tag{2.31}$$

Here T_λ is the temperature at the edge of the Knudsen layer, i.e., one mean free path (λ) away from the wall.

2.3.2 General Slip Condition

The expansion originally given in (Schaaf and Chambre, 1961) is of first order in Kn. However, for higher Knudsen numbers, second-order corrections to these boundary conditions may become necessary. The velocity slip near the wall is coupled with the first and second variations of the tangential velocity in the normal direction to the wall. Numerical implementation of the slip formula in this form is computationally difficult. Therefore, further simplification of (2.28) without changing the second-order dependence on Kn is desired. For this purpose we assume that the transition from no-slip flow to slip flow occurs smoothly. Thus, a regular perturbation expansion of the velocity field in terms of Kn is defined in equation (2.32) below, where the no-slip Navier–Stokes velocity field is denoted by $U_0(\mathbf{x}, \mathbf{t})$, and corrections to the velocity field due to different orders of Kn dependence are denoted by $U_i(\mathbf{x}, \mathbf{t})$ $(i = 1, 2, 3 \ldots)$. We then have

$$U = U_0 + \mathrm{Kn}\, U_1 + \mathrm{Kn}^2\, U_2 + \mathrm{Kn}^3\, U_3 + \mathcal{O}(\mathrm{Kn}^4). \tag{2.32}$$

This substitution enables us to rewrite the Navier–Stokes equations for different orders of Kn dependence in the following form:

$$
\begin{aligned}
\mathcal{O}(1): \quad & \frac{\partial \mathbf{U}_0}{\partial t} + (\mathbf{U}_0 \cdot \nabla)\mathbf{U}_0 = -\nabla P_0 + \mathrm{Re}^{-1}\nabla^2 \mathbf{U}_0; \\
\mathcal{O}(\mathrm{Kn}): \quad & \frac{\partial \mathbf{U}_1}{\partial t} + (\mathbf{U}_1 \cdot \nabla)\mathbf{U}_0 + (\mathbf{U}_0 \cdot \nabla)\mathbf{U}_1 = -\nabla P_1 + \mathrm{Re}^{-1}\nabla^2 \mathbf{U}_1; \\
\mathcal{O}(\mathrm{Kn}^2): \quad & \frac{\partial \mathbf{U}_2}{\partial t} + (\mathbf{U}_0 \cdot \nabla)\mathbf{U}_2 + (\mathbf{U}_2 \cdot \nabla)\mathbf{U}_0 + (\mathbf{U}_1 \cdot \nabla \mathbf{U}_1) \\
& = -\nabla P_2 + Re^{-1}\nabla^2 \mathbf{U}_2; \\
\mathcal{O}(Kn^3): \quad & \frac{\partial \mathbf{U}_3}{\partial t} + (\mathbf{U}_0 \cdot \nabla)\mathbf{U}_3 + (\mathbf{U}_3 \cdot \nabla)\mathbf{U}_0 + (\mathbf{U}_2 \cdot \nabla)\mathbf{U}_1 \\
& + (\mathbf{U}_1 \cdot \nabla)\mathbf{U}_2 = -\nabla P_3 + \mathrm{Re}^{-1}\nabla^2 \mathbf{U}_3.
\end{aligned} \tag{2.33}
$$

The boundary conditions for these equations are obtained similarly by substitution of the asymptotic expansion into the slip boundary condition formula:

$$
\begin{aligned}
\mathcal{O}(1): \quad & U_0|_s = U_w, \\
\mathcal{O}(Kn): \quad & U_1|_s = \frac{2-\sigma}{\sigma}(U_0')\Big|_s, \\
\mathcal{O}(Kn^2): \quad & U_2|_s = \frac{2-\sigma}{\sigma}\left(\frac{1}{2}U_0'' + U_1'\right)|_s, \\
\mathcal{O}(Kn^3): \quad & U_3|_s = \frac{2-\sigma}{\sigma}\left(U_2' + \frac{1}{2}U_1'' + \frac{1}{6}U_0'''\right)\Big|_s,
\end{aligned} \tag{2.34}
$$

where U_i', U_i'', and U_i''' denote first, second, and third derivatives of the ith-order tangential velocity field along the normal direction to the surface.

A possible solution methodology for slip flow with high-order boundary conditions can be the solution of the Navier–Stokes equations ordee by order. However, this approach is computationally expensive, and there are numerical difficulties associated with accurate calculation of higher-order derivatives of velocity near walls with an arbitrary surface curvature.

We propose a formulation where the governing equations are directly solved without an asymptotic expansion in velocity, as mentioned above. The objective is to establish a methodology to develop slip boundary conditions accurate up to the second-order terms in Kn. First, we introduce a **new slip boundary condition**

$$
U_s - U_w = \frac{2-\sigma_v}{\sigma_v}\frac{\mathrm{Kn}}{1 - B(\mathrm{Kn})\ \mathrm{Kn}}\left(\frac{\partial U}{\partial n}\right), \tag{2.35}
$$

where $B(\mathrm{Kn})$ is an empirical parameter to be determined. For a general choice of $B(\mathrm{Kn})$, equation (2.35) is first-order accurate in Kn, provided that $|B(\mathrm{Kn})| < 1$. However, for the continuum flow regime ($\mathrm{Kn} \to 0.0$)

the parameter $B(\mathrm{Kn})$ has a definite value. This value can be used to make equation (2.35) second-order accurate in Kn for finite Kn. For the rest of the Kn values, $B(\mathrm{Kn})$ can be curve-fitted accurately using the solutions of corresponding numerical models (i.e., Navier–Stokes and DSMC models) for the entire Kn range ($0.0 < \mathrm{Kn} < \infty$). Equation (2.35) suggests finite corrections for slip effects for the entire Kn range, provided that $B(\mathrm{Kn}) \leq 0$. It is possible to obtain the value of the parameter $B(\mathrm{Kn})$ for small Kn, especially for the slip flow regime, by Taylor series expansion of $B(\mathrm{Kn})$ about $\mathrm{Kn} = 0$. We thus obtain

$$B(\mathrm{Kn}) = B|_0 + \left.\frac{dB}{d\,\mathrm{Kn}}\right|_0 \mathrm{Kn} + \cdots = b + \mathrm{Kn}\ c + \cdots. \tag{2.36}$$

Assuming that $|B(\mathrm{Kn})| < 1$, we expand equation (2.35) in geometric series, including also the expansion given in equation (2.36) for $B(\mathrm{Kn})$. This results in

$$U_s - U_w = \frac{2-\sigma_v}{\sigma_v}\,\mathrm{Kn}\,\frac{\partial U}{\partial n}[1 + b\,\mathrm{Kn} + (b^2 + c)\,\mathrm{Kn}^2 + \cdots]. \tag{2.37}$$

Next, we substitute the asymptotic expansion for the velocity field (equation (2.32)) to the general slip condition given above, and rearrange the terms as a function of their Knudsen number order. This results in

$$\begin{aligned}
\mathcal{O}(1): &\quad U_0|_s = U_w; \\
\mathcal{O}(\mathrm{Kn}): &\quad U_1|_s = \frac{2-\sigma_v}{\sigma_v}(U_0')|_s; \\
\mathcal{O}(\mathrm{Kn}^2): &\quad U_2|_s = \frac{2-\sigma_v}{\sigma_v}(bU_0' + U_1')|_s; \\
\mathcal{O}(\mathrm{Kn}^3): &\quad U_3|_s = \frac{2-\sigma_v}{\sigma_v}(U_2' + bU_1' + (b^2+c)U_0')|_s.
\end{aligned} \tag{2.38}$$

Comparing these equations with the conditions obtained from the Taylor series expansion in equation (2.35) order by order, we obtain that the two representations are identical up to the first-order terms in Kn. To match the second-order terms we must choose the parameter b as

$$b = \left(\frac{1}{2}\frac{U_0''}{U_0'}\right)_s = \frac{1}{2}\left[\frac{\left(\frac{\partial \omega}{\partial n}\right)_0}{\omega_0}\right]_s. \tag{2.39}$$

The quantities U_0' and U_0'' for an arbitrary curved surface denote first and second derivatives of the tangential component of the velocity vector along the normal direction to the surface, corresponding to a *no-slip* solution.

- *The parameter b in equation (2.39) is the ratio of the vorticity flux to the wall vorticity, obtained in no-slip flow conditions. The value of b for simple flows can be found analytically.*

Similarly, third-order terms in Kn can be matched if c is chosen as

$$c = \frac{1}{U_0'}\left(\frac{1}{2}U_1'' + \frac{1}{6}U_0''' - b^2 - bU_1'\right). \tag{2.40}$$

However, the third-order-accurate slip formula is computationally more expensive, since it requires the solutions for the U_1 field. We can obtain a second-order-accurate slip formula by approximating equation (2.35) as

$$U_s - U_w = \frac{2-\sigma_v}{\sigma_v}\frac{\mathrm{Kn}}{1 - B\,\mathrm{Kn}}\frac{\partial U}{\partial n} = \frac{2-\sigma_v}{\sigma_v}\frac{\mathrm{Kn}}{1 - b\,\mathrm{Kn}}\frac{\partial U}{\partial n} + \mathcal{O}(\mathrm{Kn}^3), \tag{2.41}$$

where b is the high-order slip coefficient given in equation (2.39). The error for equation (2.41) is $\mathcal{O}(\mathrm{Kn}^3)$, i.e.,

$$\text{Error } = c\,U_0'\,\mathrm{Kn}^3\,.$$

Truncated geometric series containing only $\mathcal{O}(\mathrm{Kn}^2)$ terms could have also been used to implement the new second-order slip-boundary condition (see equation (2.37)). The error in this case is also $\mathcal{O}(\mathrm{Kn}^3)$, and is given as

$$\text{Error}_{g.s.} = [U_2' + bU_1' + (b^2 + c]U_0')\,\mathrm{Kn}^3\,.$$

Since we do not know the magnitude of the U_1' and U_2' terms, it is difficult to decide which approach is better. However, we believe that using equation (2.41) is better, since this equation keeps the original form suggested in (2.35). Also for separated flows, equation (2.41) gives no slip at the separation or reattachment points (as predicted from the first-order slip formula), since the shear stress (therefore $\frac{\partial U}{\partial n} = 0$) is zero at these points. However, the truncated geometric series (equation (2.37)) will give multiplication of infinitesimally small wall shear stress ($\tau_{\text{wall}} = \mu\frac{\partial U}{\partial y} \to 0.0$) with large b ($b = \frac{U_o''}{2U_o'} \to \infty$, since $U_o' \to 0$). This may result in a velocity slip at the separation point based on some numerical truncation error in the calculations.

In this section we have developed various second- and higher-order slip conditions for gas microflows. We note that the Navier–Stokes equations require only the first-order slip conditions, and the second-order slip models should be used strictly for the second-order equations, such as the Burnett or Woods equations. Throughout this book we will utilize the second-order slip conditions routinely for the Navier–Stokes equations. This can be justified by the following arguments:

TABLE 2.2. Coefficients for first- and second-order slip models.

Author	C_1	C_2
Cercignani (Cercignani and Daneri, 1963)	1.1466	0.9756
Cercignani (Hadjiconstantinou, 2003a)	1.1466	0.647
Deissler (Deissler, 1964)	1.0	9/8
Schamberg (Schamberg, 1947)	1.0	$5\pi/12$
Hsia and Domoto (Hsia and Domoto, 1983)	1.0	0.5
Maxwell (Kennard, 1938)	1.0	0.0
Equation (2.29)	1.0	-0.5

- In the small Reynolds number limit, i.e., $\mathrm{Re} \ll \mathrm{Kn} \ll 1$, asymptotic analysis of the Boltzmann equation shows that a consistent set of governing equations and boundary conditions up to $\mathcal{O}(\mathrm{Kn}^2)$ is the Stokes system with second-order slip boundary conditions; see Section 15.4.2 and for details (Sone, 2002; Aoki, 2001).
- Rarefaction effects both in the aforementioned limit as well as in the limit of $\mathrm{Re} \sim \mathcal{O}(1) \rightarrow M \sim \mathcal{O}(Kn)$ come in only through the boundary condition. This has been proven rigorously using the Boltzmann equation in (Sone, 2002).
- The high-order boundary conditions proposed include Maxwell's first-order slip conditions (2.19), (2.19) as the leading-order term. Hence, these results are correct up to $\mathcal{O}(\mathrm{Kn})$ in the slip flow regime, irrespective of the formal order of the utilized slip conditions.
- The general boundary condition for slip (equation (2.43)) converges to a finite value for large Kn, unlike the first-order Maxwell's boundary condition.

2.3.3 Comparison of Slip Models

For isothermal flows with tangential momentum accommodation coefficient $\sigma_v = 1$, the general second-order slip condition has the *nondimensional* form

$$U_s - U_w = C_1 \,\mathrm{Kn} \left(\frac{\partial U}{\partial n}\right)_s - C_2 \,\mathrm{Kn}^2 \left(\frac{\partial^2 U}{\partial n^2}\right)_s , \tag{2.42}$$

where $(\partial/\partial n)$ denotes gradients normal to the wall surface. The coefficients C_1 and C_2 are the slip coefficients. Typical values of the slip coefficients developed by different investigators are shown in Table 2.2.

We will apply the second-order slip boundary conditions given above for channel flows in Chapter 4 to examine their accuracy in representing the flow profile, including the velocity slip predictions. According to Sreekanth

(Sreekanth, 1969), Cercignani's second-order boundary conditions should be used only for evaluating the flow states *far from the wall*, and these conditions should not be used to evaluate space integrals in regions extending close to the walls. Sreekanth reports good agreement of second-order slip boundary conditions with his experimental results for Kn as high as Kn = 1.5 (Sreekanth, 1969). However, Sreekanth used a different second-order slip coefficient ($C_2 = 0.14$) than the original ones shown in Table 2.2. He also reports a change of the first slip coefficient (C_1) from 1.00 to 1.1466 as the Knudsen number is increased. First-order boundary conditions cease to be accurate, according to Sreekanth's study, above Kn > 0.13. More recent studies also show that Maxwell's slip boundary condition breaks down around Kn = 0.15 (Piekos and Breuer, 1995).

Implementation of second-order slip boundary conditions using equation (2.29) requires obtaining the second derivative of the tangential velocity in the normal direction to the surface ($\partial^2 U/\partial n^2$), which may lead to computational difficulties, especially in complex geometric configurations. To circumvent this difficulty we have proposed in the previous section the following *general* velocity slip boundary condition.

$$U_s - U_w = \frac{2-\sigma_v}{\sigma_v}\left[\frac{\mathrm{Kn}}{1-b\,\mathrm{Kn}}\left(\frac{\partial U}{\partial n}\right)_s\right], \tag{2.43}$$

where b is a general slip coefficient. Notice that the value of b can be determined such that for $|b\,\mathrm{Kn}\,| < 1$ the geometric series obtained from the boundary condition of equation (2.43) matches exactly the second-order equation (2.29), and thus for slip flow the above boundary condition is *second-order accurate* in the Knudsen number.

An alternative way of implementing the slip boundary condition is to use equation (2.26) derived directly from the tangential momentum flux analysis. Such a boundary condition has not been tested before, so in Section 4.1.3 we will determine the region of its validity, and in particular at what distance from the wall it should be applied, i.e., λ or $C\lambda$, where $C \neq 1$ (see Figure 2.5 and (Thompson and Owens, 1975)).

As regards the accuracy of two velocity slip boundary conditions, i.e., equation (2.26) versus equation (2.43), we can analyze the differences for the two-dimensional pressure-driven incompressible flow between parallel plates separated by a distance h in the slip-flow regime. Assuming isothermal conditions and that the slip is given by equation (2.26), the corresponding velocity distribution is

$$U(y) = \frac{h^2}{2\mu}\frac{dP}{dx}\left[\frac{y^2}{h^2} - \frac{y}{h} - \frac{2-\sigma_v}{\sigma_v}(\mathrm{Kn} - \mathrm{Kn}^2)\right]. \tag{2.44}$$

This is identical to the results obtained using equation (2.43) up to second-

order terms in Kn, given below:

$$U(y) = \frac{h^2}{2\mu}\frac{dP}{dx}\left[\frac{y^2}{h^2} - \frac{y}{h} - \frac{2-\sigma_v}{\sigma_v}\frac{\mathrm{Kn}}{1+\mathrm{Kn}}\right]. \tag{2.45}$$

This equivalence can be seen by expanding the last term in equation (2.45) as a geometric series expansion in terms of powers of Kn. The leading error in equation (2.45) is therefore proportional to

$$\frac{h^2}{2\mu}\left|\frac{\partial P}{\partial x}\right| \mathrm{Kn}^3,$$

where h is the microchannel height.

Remarks: We summarize here observations that will aid in evaluating the proper application and limitations of the slip boundary conditions given by equations (2.42) and (2.43).

1. The first-order slip boundary condition should be used for $\mathrm{Kn} \leq 0.1$ flows. Since rarefaction effects gradually become important with increased Kn (regular perturbation problem), inclusion of second- and higher-order slip effects into a Navier–Stokes–based numerical model is neither mathematically nor physically inconsistent.

2. Using the high-order slip boundary conditions with the Navier–Stokes equations can lead to some physical insight. For example, using equation (2.42) for pressure-driven flows with various slip coefficients from Table 2.2 results in different velocity profile and flowrate trends. All the models in Table 2.2, with the exception of equation (2.29), result in *increased flowrate* due to the second-order slip terms. Although this is a correct trend for flowrate, the velocity distribution predicted by these models become erroneous with increased Kn, as shown in Figures 4.11 and 4.17. This indicates that *solely using the high-order slip correction in the transition flow regime is insufficient to predict the velocity profile and the flowrate simultaneously.* In Section 4.2, we address this problem by introducing a *rarefaction correction parameter* that leads to a unified flow model for pressure-driven channel and pipe flows, when combined with the *general* slip condition (equation (2.43)). The unified model predicts the correct velocity profile, flowrate, and pressure distribution in the *entire Knudsen regime* (see Section 4.2 for details).

3. Steady plane Couette flows have linear velocity profiles, which result in $\partial^2 U/\partial n^2 = 0$. Therefore, the high-order slip effects in equations (2.42) and (2.43) diminish for plane Couette flows. In Section 3.2, we demonstrate a generalized slip model for linear Couette flows that is valid for $\mathrm{Kn} \leq 12$.

4. As a final remark, interfacial interactions between the gas and surface molecules may result in inelastic reflections, due to the long-range interaction forces between the gas and surface molecules. Consequently, the gas molecules may condense and then evaporate after a certain time. This results in deposition of a thin layer of gas molecules on the surface. Using Langmuir's theory of adsorption, Myong (2004) explained the accommodation coefficient concept, and studied velocity slip for both monatomic and diatomic molecules. He has shown that the Langmuir model recovers Maxwell's first-order slip conditions, and he also described equation (2.43) in the context of the Langmuir model (Myong, 2004).